Tuning the Bi^{3+}-photoemission color over the entire visible region by manipulating secondary cations modulation in the $ScV_xP_{1-x}O_4:Bi^{3+}$ ($0 \le x \le 1$) solid solution

Kang, Fengwen; Sun, Guohuan; Boutinaud, Philippe; Gao, Fei; Wang, Zhenhu; Lu, Jian; Li, Yang Yang; Xiao, Sanshui

Published in:
Journal of Materials Chemistry C

Link to article, DOI:
10.1039/c9tc01385g

Publication date:
2019

Document Version
Peer reviewed version

Tuning the Bi^{3+}-photoemission color over the whole visible region through manipulating secondary cations modulation in the $ScV_xP_{1-x}O_4:Bi^{3+}$ ($0 \leq x \leq 1$) solid solution

Fengwen Kang,[a,d,e,f,g,*] Guohuan Sun,[b] Philippe Boutinaud,[c] Fei Gao,[d] Zhenhu Wang,[k] Jian Lu,[e,f,g,h,] Yang Yang Li,[g,h,i,j,] and Sanshui Xiao,[a*]

[a] DTU Fotonik, Department of Photonics Engineering, Technical University of Denmark, Anker Engelunds Vej 1, 2800 Kgs, Lyngby, Denmark; [b] The State Key Laboratory of Experimental Hematology, Institute of Hematology, Chinese Academy of Medical Sciences, Nanjing Road No. 288, Tianjin 300020, China; [c] Clermont Université Auvergne, SIGMA Clermont, Institut de Chimie de Clermont-Ferrand, BP 10448, 63000 Clermont-Ferrand, France; [d] Department of Physics, Department of Micro- and Nanotechnology, Technical University of Denmark (DTU), Anker Engelunds Vej 1, 2800 Kgs, Lyngby, Denmark; [e] Center of Super-Diamond and Advanced Films (COSDAF), City University of Hong Kong, 83 Tat Chee Avenue, Kowloon, Hong Kong, China; [f] Hong Kong Branch of National Precious Metals Material Engineering Research Centre, City University of Hong Kong, 83 Tat Chee Avenue, Kowloon, Hong Kong, China; [g] Department of Materials Science and Engineering, City University of Hong Kong, 83 Tat Chee Avenue, Kowloon, Hong Kong, China; [h] Department of Mechanical Engineering, City University of Hong Kong, 83 Tat Chee Avenue 83, Kowloon, Hong Kong, China; [f] Institute of Hematology, Chinese Academy of Medical Sciences, Tianjin, China; [i] Centre for Advanced Structural Materials, City University of Hong Kong Shenzhen Research Institute, 8 Yuexing 1st Road, Shenzhen Hi-Tech Industrial Park, Nanshan District, Shenzhen, China; [j] Clermont Université Auvergne, SIGMA Clermont, Institut de Chimie de Clermont-Ferrand, BP 10448, 63000 Clermont-Ferrand, France; [k] Fundamental Science on Nuclear Wastes and Environmental Safety Laboratory, Southwest University of Science and Technology, Mianyang, China.

ABSTRACT

Unlike the rare earth (RE) (*e.g.*, Eu^{2+}) and non-RE (*e.g.*, Mn^{2+}) doped tunable solid solutions that frequently suffer from the visible re-absorption issue, the Bi^{3+} ion features remarkable advantages of strong UV excitation intensity and excitation tail less than 430 nm, allowing the Bi^{3+} to have strong ability of solving the re-absorption issue for future lighting technology. Herein, we report a type of zircon-type $ScV_xP_{1-x}O_4:Bi^{3+}$ ($0 \leq x \leq 1$) emission-tunable solid solution that has a strong UV excitation intensity yet no significant light absorption. We reveal that gradual substitution of larger V ions for smaller P ions, which means expansion of lattice cell, can shift the excitation edge from 295 nm to 385 nm, excitation tail from 340 nm to 425 nm and emission position from 455 nm to 641 nm, without big change of the Stokes shift. This spectral shifting is found to be the consequence of a complex dependence of intra-ion and charge-transfer related transitions of Bi^{3+} with the crystal structure. Because of the remarkable excitation-triggered multi-emission properties, we discover further that the $ScV_xP_{1-x}O_4:Bi^{3+}$ solid solution can serve as a type of potential material for anti-counterfeiting and information protection applications. This work enables providing some design insights into discovering more RE and non-RE doped tunable solid solutions in the future, through modulating the secondary cations in the isostructural crystals.

Key words: Bi^{3+}; tunable solid solution; fluorescence; anti-counterfeiting; phospho-vanadates.

Corresponding authors

Email: kangfengwen0597@126.com; and saxi@fotonik.dtu.dk

1. Introduction

Spectrally tunable solid solutions based on rare earth (RE) and non-RE doping are a type of highly important phosphor materials in the solid-state lighting technology, which enable device designers to benefit the flexible color-emitting choices but not to consider the complicated lighting system design and integration and the color imbalance problem that results from different responses of different phosphors to variation of external factors such as the LED chip temperature [1-5]. The emission-tunable approaches used for achieving the solid solutions have been widely described in the archival literatures, but strategies are usually focused on isostructural crystals that incorporate dopants like Eu^{2+} [6], Ce^{3+} [7], Mn^{2+} [8], and Bi^{3+} [9] ions whose spectral characteristics are very sensitive to the nature of their nearby chemical microenvironment, owing to the outer character of the emitting states. As a matter of comparison, the well-shielded 4*f* ions (*e.g.*, Eu^{3+} [10], Pr^{3+} [11], Tb^{3+} [12], Tm^{3+} [13], Er^{3+} [14-15] *etc*) and other 3*d* ions like Mn^{4+} [16], and Cr^{3+} [17]) usually exhibit their fixed spectral shape and positions, making the tunable-emission being less to realize in single ion doped solid solutions.

In most cases, realization of single Eu^{2+}, Ce^{3+}, Bi^{3+}, or Mn^{2+} ion doped tunable solid solutions is based upon how to manipulate isostructural ions that feature the same valence but different radii at the same coordination number (CN). For example, Ji *et al* reported the Ce^{3+} tunable emission in the $Ba_{2-x}Sr_xSiO_4:Ce^{3+}$ ($x = 0 \rightarrow 1.8$, $\lambda_{em} = 391 \rightarrow 411$ nm) [18]; Fu *et al* reported the Eu^{2+} tunable emission in the $Sr_{2.97-x}Ba_xMgSi_2O_8:Eu^{2+},Dy^{3+}$ ($x = 0 \rightarrow 2.0$, $\lambda_{em} = 434 \rightarrow 464$ nm) [19]; Dai *et al* showed the Eu^{2+} tunable emission in the $(K_{1-x},Na_x)SrPO_4:Eu^{2+}$ ($x = 0 \rightarrow 0.6$, $\lambda_{em} = 446 \rightarrow 498$ nm) [20]; Zhang *et al* realized and presented the Mn^{2+} tunable emission in the $(Ca_{1-a}Sr_a)_{10}Li(PO_4)_7:0.09Mn^{2+}$ ($a = 0 \rightarrow 0.4$, $\lambda_{em} = 642 \rightarrow 632$ nm) [21]; and Kang *et al* recently reported the $(Y_x,Lu_y,Sc_z)VO_4:Bi^{3+}$ ($x \rightarrow y \rightarrow z$; $\lambda_{em} = 566 \rightarrow 576 \rightarrow 635$ nm) tunable solid solution [22]. Besides, exemplarily basing upon other reported tunable solid solutions [23-28], it is found further that the isostructural ions involved for modifying the local microenvironments fall into two types, *i.e.*, (**i**) those ions that can be replaced by the dopants, and (**ii**) those ions that are not involved in the dopant substitution. The former type (**i**), for example, in the solid solutions of $Sr_{2.97-x}Ba_xMgSi_2O_8:Eu^{2+},Dy^{3+}$ [19], $Sr_{3-x}Ba_xMgSi_2O_8:Eu^{2+}$ [27], and $(Sr_{1-x},Ba_x)P_4O_{13}:Eu^{2+}$ [28], features two type of isostructural cations in their intermediate phases that are available for the dopants substitution. In this way, if one wanted to know the intrinsic tunable nature, it has to take into account the site occupancy preferential problem. Although several views have been proposed to explain the intrinsic tunable nature (*e.g.*, the crystal field modulation in $(K_{1-x},Na_x)SrPO_4:Eu^{2+}$ [20]), but the final emission bands cannot be excluded from an integrated contribution of multiple emission bands.

Almost all of the reported works seem to be lack of their care to this aspect of tunable luminescence that is associated with a deep-seated issue that involves the distribution and re-distribution of dopant in different isostructural crystal sites. As for type (**ii**), since the tunable solid solutions involve only a type of crystal sites for the dopant, the question of site occupancy preference is not so critical, like in the $Sr_8Mg_{1-m}Zn_mY(PO_4)_7:Eu^{2+}$ [29].

Significantly, among the Eu^{2+}, Ce^{3+}, Bi^{3+}, and Mn^{2+} ions, previous reports concerning single Eu^{2+}, Ce^{3+}, or Mn^{2+} ion doped tunable solid solutions are seen more often than that involving single Bi^{3+} solid solutions. As for the Eu^{2+}, Ce^{3+}, and Mn^{2+} ions, however, one major drawback is the evitable light re-absorption problem in the visible spectral region. Over the past years, a number of works had pointed out the necessity of solving this problem [22, 30-37], but it seems that the *d-f* (*i.e.*, for Eu^{2+}, and Ce^{3+}) and $^4T_1(^4G) \rightarrow {}^6A_1(^6S)$ (*i.e.*, for Mn^{2+}) transitions feature an inherently-inviolable law, making them impossible to have the tunable-emission and non-visible re-absorption at the same time. By contrast, a dopant like Bi^{3+} ion could be relevant to address well this point [22, 32, 35-36]. Because of a naked 6*s* electron in the electronic configuration of $[Xe]\text{-}4f^{14}5d^{10}6s^2$ [22, 32-33, 35-38], the Bi^{3+} ion, depending on the specific crystal host it built into, can present the emissions broadly spanning from the UV [39], blue [40], yellow [41] and to reddish/red region [35, 32-33, 42], which are analogous to the Eu^{2+}, Ce^{3+}, and Mn^{2+} ions. As compared to the frequently reported Eu^{2+}, Ce^{3+}, and Mn^{2+} tunable solid solutions, however, only a very limited examples of Bi^{3+} emission solid solutions have been reported in the literatures, such as $(Y_x,Lu_y,Sc_z)VO_4:Bi^{3+}$ (yellow → reddish/red) [22], $Ba_{3-x}Sr_xSc_4O_9:Bi^{3+}$ (blue → green) [43], and $YP_xV_{1-x}O_4:Bi^{3+}$ (blue → yellow) [44]. Typically, there are still no literatures that have reported the existence of Bi^{3+} doped tunable solid solutions that can show their emissions cover the whole visible spectral region,

Besides, works concerning the luminescent phosphor materials have been widely reported for the solid-state lighting technology such as phosphor-converted white LEDs. Sometimes, some works also propose the phosphor materials for the anti-counterfeiting applications. For example, Chen *et al* reported that the $(Y,Gd)VO_4:Bi^{3+},Eu^{3+}$ phosphor featured temperature-sensitive luminescence properties and proved it could be used for stealth anti-counterfeiting [45], but the emission tuning come from an integrated emission of Eu^{3+} and Bi^{3+} ions due to the inefficiency energy transfer from Bi^{3+} to Eu^{3+} ions. Moreover, this phosphor has two types of crystal sites (*i.e.*, Y, and Gd) for Bi^{3+} and Eu^{3+} substitution and, thus, involves the complicated site occupy preferential problem. Furthermore, it is found that the Bi^{3+} emission positions as the Y/Gd ratios change did not change in the $(Y,Gd)VO_4:Bi^{3+},Eu^{3+}$ [45-46]. In some already-reported cases, the Bi^{3+} ion is also reported to serve as a role of "sensitizer" to improve the luminescence intensity of RE (*e.g.*, Eu^{3+} [2, 45-46],

Tb^{3+} [47], Tm^{3+} [48] *etc*) and non-RE (*e.g.*, Mn^{4+} [49-50] *etc*) ions. With temporal fluorescence change like in the $(Y,Gd)VO_4:Bi^{3+},Eu^{3+}$ [45-46], the anti-counterfeiting applications are proposed. Some other phosphors like the $SiO_2@SrTiO_3:Eu^{3+},Li^+$ [51], $Y_2O_3:Eu^{3+}$ [52], and Tb^{3+},Eu^{3+}-Doped Strontium-Aluminum Chlorites [53] have been also proposed for anti-counterfeiting applications. All of these phosphors, however, do not belong to the category of the tunable solid solutions. In addition, their relevant anti-counterfeiting applications actually cannot work without using the RE as the luminescent center. Thus, exploring non-RE doped solid solutions that can use for temporal data storage, information encryption and anti-counterfeiting applications is very meaningful.

To jointly answer the above issues, we designed and reported on the zircon-type $ScV_xP_{1-x}O_4:Bi^{3+}$ ($0 \leq x \leq 1$) solid solution that enabled featuring strong UV excitation intensity with no significant re-absorption in the visible spectral region and emission positions that were broadly tuned over the whole visible region. The intrinsic processes, which gave rise to the progressive shift of the Bi^{3+} excitation edge from 295 nm to 385 nm, excitation tail from 340 nm to 425 nm and concomitant emission tuning from 455 nm to 641 nm as we gradually moved from $ScPO_4:Bi^{3+}$ to $ScVO_4:Bi^{3+}$, had been carefully discussed basing upon Rietveld refinements, and semi-empirical models. Such unique spectral properties were discovered to make this type of Bi^{3+} solid solution favorable candidate for anti-counterfeiting and information protection applications.

2. Experimental Details

2.1 Samples synthesis

Solid solution compounds with nominal chemical composition, *i.e.*, $Sc_{0.98}(V_x,P_{1-x})O_4:Bi_{0.02}{}^{3+}$ ($0 \leq x \leq 1$, with x varying by steps of 0.2), were prepared by high temperature solid state reaction using Sc_2O_3 (99.95%), $NH_4H_2PO_4$ (99.999%), NH_4VO_3 (99.95%), and Bi_2O_3 (99.9%) as raw chemicals. All the stoichiometric mixtures were fired at 1200 ^oC for 3 h in air. To avoid the volatilization of raw chemicals, the heating rate was set to 3 ^oC per minute.

2.2 Characterizations

The powder X-ray diffraction (XRD) patterns were recorded by a Bruker D8 ADVANCE powder diffractometer operated at 40 kV, 40 mA, and $1.2°\cdot min^{-1}$ with the $Cu_{K\alpha}$ radiation (λ = 1.54059 Å). A Hitachi F-7000 fluorescence spectrophotometer with a *Xe* lamp as excitation source was used to collect the photoluminescence (PL) spectra at room temperature. In order to precisely achieve the luminescence intensity upon composition and excitation wavelength, the emission and excitation slits and the scanning rate were set to 3.0 nm and 240 nm/min, respectively. The excitation light source utilized for illustrating the anti-counterfeiting and information protection applications was also from the Hitachi F-7000 fluorescence spectrophotometer.

3. Theoretical Details

Our first-principles calculations were performed within framework of density functional theory (DFT) using the Vienna *ab* initio simulation package (VASP) [54-55]. The projected augmented wave (PAW) [56] potentials were adopted with the valence states of $2s^2 2p^4/4s^2 3d^1/3d^4 4s^1/3s^2 3p^3$ for O/Sc/V/P, respectively. A plane wave cutoff of 500 eV was used to expand the wave function. The total energy was converged to a level of 0.0001 eV during the self-consistent electron density optimization. All atoms were allowed to relax until the forces on each atom had magnitude less than 0.01 eV $Å^{-1}$. The Brillouin zone was sampled using the Monkhorst-Pack scheme with 4 × 4 × 4. To describe the V-P alloying, solid solution with the chemical composition of $ScV_{1-x}P_xO_4$ (x = 0, 0.25, 0.5, 0.75, and 1.0) were modeled using the enumerated configurations and super-lattices generated by the Hermite Normal Form (HNF) matrices size of one, two, three, four times than primitive cells, where the degeneracy of each inequivalent configuration was obtained.

4. Results and Discussion

4.1 Electronic bandgap properties of $ScV_{1-x}P_xO_4$

Kang *et al* [36] and Cavalli *et al* [44] found respectively in $YV_xNb_{1-x}O_4$ and $YV_xP_{1-x}O_4$ that the electronic band gap (E_g) as the V/Nb and P/V ratios change can change regularly, which have been proved to use as the fundamental basis of initial consideration to realize the Bi^{3+} spectral tuning in the $YV_xNb_{1-x}O_4:Bi^{3+}$ and $YV_xP_{1-x}O_4:Bi^{3+}$ solid solution. In light of this, we therefore calculated the E_g values of bulk $ScV_xP_{1-x}O_4$ ($0.0 \leq x \leq 1$) using the DFT calculations. It is shown in **Figure 1a** that the E_g values as the V/P increases are decreased from 4.11 eV (*i.e.*, x = 0.0) to 2.56 eV (*i.e.*, x = 1.0). Notice that the E_g values of intermediate $Sc(V_x,P_{1-x})O_4$ (*i.e.*, x = 0.25, 0.50, 0.75) solid solution were calculated basing upon a homogeneous substitution of smaller P ions with lager V ions and without considering the defects such as the oxygen vacancy. **Figure 1b** gives a typical crystal structure we modeled, *i.e.*, the intermediate $ScV_{0.5}P_{0.5}O_4$ compound. The E_g value of 4.11 eV in $ScPO_4$ significantly differs in the experimental E_g value of 7.2 eV reported by Trukhin A *et al* [57], but it is more close to those values calculated by DFT modeling (**Table 1**) [58-60]. Noticing in **Table 1** reveals that different DFT modeling methods always lead to different E_g values [58-60, 33, 62-66] of $ScPO_4$ and $ScVO_4$. However, as compared to the experimental E_g values [33, 57-66], the theoretical E_g values from DFT are obviously underestimated. Such scenarios are frequently reported in previous works like in *refs*. [33, 62]. Under this consideration, the theoretical E_g values of 4.11 eV in $ScPO_4$ and 2.56 eV in $ScVO_4$ are reasonable, although they are underestimated as

compared to the experimental E_g values of 7.2 eV, 7.73 eV and 6.73 eV in $ScPO_4$ [57] and 2.8 eV in an oxygen-free $ScVO_4$ [37]. Anyway, the regular decrease of variation tendency of E_g values in $ScV_xP_{1-x}O_4$ (**Figure 1b**) would be a consideration basis to predict the existence of the Bi^{3+} spectral tuning if one could form the $ScV_xP_{1-x}O_4$:Bi^{3+} solid solution.

4.2 Analysis on structural properties

The inorganic oxide compounds, shared with the crystallographic structure of $LnBO_4$ (where Ln denotes lanthanide ions; B represents P, V, and Nb ions), are attractive for trivalent ion substitution (*e.g.*, Bi^{3+} [36-40, 44, 45], Eu^{3+} [45, 67], and Tm^{3+} [48]). Among the $LnBO_4$ system, the $ScVO_4$ and $ScPO_4$ crystallize with the zircon-type $I4_1/amd$ structure consisting of interconnected [ScO_8] bisphenoids and [BO_4] (B = P, V) tetrahedra (**Figure 1c**). The [ScO_8] and [BO_4] structures are closely linked with each other by sharing either edge or oxygen atoms, leading to formation of the Sc···O···B (B = P, V) chain. Moreover, there is only one type of Sc^{3+} site available for Bi^{3+} dopant in the lattices, but two type of B-O bonds appear in the $ScPO_4$ and $ScVO_4$, respectively. Once an amount of Bi^{3+} dopants were built into the crystal lattices, it would be expected to change parts of the Sc···O···B (B = P, V) chains into the Bi···O···B (B = P, V) chains.

As depicted in **Figure 2**, gradual substitution of P^{5+} ions with V^{5+} ions does not induce the detectable impurity phase, but brings about a continuous series of solid solution with a progressive shift of XRD position toward low angle direction because of the ionic radii mismatch between the P^{5+} and V^{5+} ions in four-fold coordination [68-69], such as, the shift of (112) plane from 36.536° to 34.671° (**Table 2**). The splitting of XRD peaks in **Figure 2** is produced by the incoming $K_{\alpha1}$ and $K_{\alpha2}$ radiations.

Besides, we further used the Rietveld refinement method to refine the XRD data. The desirable R_p, R_{wp}, R_{exp}, R_{Bragg}, R_F, and GOF factors (**Table 3**) reveal that Rietveld results coincide well with the experimental results. **Figure 3a** and **Figure 3b** give two typical examples of refinement profiles. In **Figure 2c**(**i-iii**) and **Table 3**, the gradual variation of the refined lattice parameters and unit cell volume as the x value increases matches nicely the *Vegards*' law [19-20], which confirms the successful formation of the continuous $ScV_xP_{1-x}O_4$:Bi^{3+} solid solution. Among these cell lattice parameters deduced from the Rietveld refinements, we retain the variation of the average Sc-O bond distance (denoted hereafter <Sc-O>) and shortest Sc-P/V distances with x as key parameters to account for the effect of the $ScV_xP_{1-x}O_4$ crystal structure on the Bi^{3+}-tunable luminescence properties, whereas the composition-dependent average V-O lengths (hereafter <V-O> accounts for the energy of the $O_{2p} \rightarrow V_{3d}$ charge transfer. All these useful data are listed in **Table 3** for further calculations.

4.3 Photoluminescence (PL) spectra

Figure 4 shows the excitation and emission spectra (**a**) of $ScV_xP_{1-x}O_4:Bi^{3+}$ ($0 \leq x \leq 1$) along with the CIE chromaticity coordinates (**b** and **c**). It is not easy for us to locate the lower maximum of their excitation spectra in **Figure 4**; therefore, we preferred to locate the position of the excitation edge that we have determined from the first derivative. The corresponding values, the wavelength positions of the corresponding emission maxima, and the Full Width at Half Maximum (FWHM) values of the emission bands are given in **Table 2** and **Table 4**.

We observe a gradual redshift of the excitation edge and emission position as the V ions gradually substitute for the P ions (*i.e.*, x increases). The redshift of emission position as x is increased in $ScV_xP_{1-x}O_4:Bi^{3+}$ is well reflected by the CIE chromaticity coordinates tuning from blue, yellow, and to red. The energy mismatch between the excitation edges and the emission maxima gives rough information on the Stokes shift (ΔS) associated with each composition of the solid solution. These ΔS values are certainly somehow underestimated. In **Table 4**, we also list the wavelengths corresponding to the cross-over between emission and excitation spectra, the purpose of which is to estimate the spectral overlap between these spectra. Notice that these data were achieved after appropriate normalization of the spectral intensities and integration of the corresponding overlapping areas. As a result, we can acquire the cross points of the excitation and the emission spectra and the percentage of emission area that overlaps the corresponding excitation spectrum (*i.e.*, the spectral overlap) (**Table 4**). The results vividly exhibit the quantitative information on the little fraction of re-absorbed emission for each member of the present solid solution. Note that the emission spectral region is interrupted at 800 nm. Hence, the light re-absorption essentially occurs in the $ScV_xP_{1-x}O_4:Bi^{3+}$ solid solution, but except for a very weak visible light re-absorption in the $ScVO_4:Bi^{3+}$ compound (*i.e.*, > 400 nm), other solid solution compounds only show the re-absorption in the near UV spectral region.

4.4 Analysis and discussion on PL properties

The excitation spectrum consists of superimposed electronic transitions with different characters. Transitions within isolated Bi^{3+} ions occur from the fundamental $^1S_0$ ground state ($6s^2$ configuration) to the excited $^3P_{0,1}$, $^3P_2$, and $^1P_1$ states (*i.e.*, $6s^16p^1$ configuration) and are denoted as A, B, and C, respectively. The spin-allowed C transition is usually intense but its wavelength is usually located far in the UV spectral region (*i.e.*, generally < 250 nm). The B transition is spin forbidden and has low intensity. The A transition has, in contrast, appreciable oscillator strength through the spin-orbit mixing that takes place between $^3P_1$ and $^1P_1$, and it forms the lower lying excitation feature. In addition, transitions with charge transfer character are also observable within Bi^{3+} pairs [70-71] and

in some oxidic lattices containing metal cations (M^{n+}) having closed-shell d^0 or d^{10} electron configuration (*i.e.*, titanates, vanadates, niobates, *etc*) [37]. Note that with a nominal Bi^{3+} doping rate of 2 mol%, the probability to form Bi^{3+}-pairs in $ScV_xP_{1-x}O_4:Bi^{3+}$ is low, allowing us not to consider this possibility of Bi^{3+}-pairs in the present work frame. However, the Bi^{3+}-to-M^{n+} transitions are usually referred as D or metal-metal charge transfer (MMCT) transitions. In Bi^{3+}-doped vanadates (*e.g.*, the $ScVO_4:Bi^{3+}$ [33]), additional excitation features belonging to the host-related $[VO_4]^{3-}$ units can appear in case of energy transfer from the host to Bi^{3+} states. At last, the unusual red luminescence and corresponding low-lying excitation in $ScVO_4:Bi^{3+}$, which are due to the presence and perturbation of an oxygen vacancy, appear in the first coordination sphere of Bi^{3+} [33]. The global situation looks rather complex, but the origin of the excitation features in the $ScV_xP_{1-x}O_4:Bi^{3+}$ solid solution can be determined using a few empirical tools. Wang *et al* reported in 2012 that the energy of A and C transitions can be estimated empirically from the knowledge of the environmental factor $he_{CN(X)}$ [72]:

$$he_{CN}(X) = \sqrt{\sum_1^{N_x} f_{c(X-L)}\alpha_{(X-L)}Q_L^2} \qquad (1)$$

For a given cationic site (X) occupied by Bi^{3+} in the host lattice, with coordination number (here, CN = 8), the quantity $he_{CN(X)}$ is connected to the nephelauxetic effect at site X and gives relevant information on the influence of the nearby chemical environment on a given Bi^{3+} ion in the lattice. The $fc_{(X-L)}$ and $\alpha_{(X-L)}$ represent respectively the fractional covalency and the volume polarization of each chemical bond separating cation X to its nearby ligands L (here L = oxygen) in binary units to which the initial host lattice is decomposed. In particular, these parameters strongly depend on the X-L distances in the crystal lattices. The procedure for crystal lattice decomposition in binary units is described by previous works [73-75] and is not reproduced here for sake of brevity. Q_L is the effective charge carried by ligand L in each given X_mL_n unit, and it can be further calculated using the expression of $Q_L = \frac{m}{n}Q_X$ (where Q_X denotes the effective charge of the considered cation X). In present work, this charge was taken as the bond valence sum of atom X in its polyhedron and was obtained from the crystal structure of the host lattice using VESTA software [76]. The necessary values of bond valence parameters were obtained from [77]. So, once $he_{CN(X)}$ is known, the energy $E_{A,CN(X)}$ in cm^{-1} of the A transition of Bi^{3+} in a given site X of a given host lattice can be obtained empirically from the following equation [72]:

$$E_{A,CN}(X) = 23970 + 50051\exp\left(-\frac{he_{CN}(X)}{0.551}\right) \qquad (2)$$

In our case, X is Sc^{3+} with 8 oxygen neighbors in the regular zircon structure of $ScV_xP_{1-x}O_4$. Owing

to the ionic mismatch between Sc^{3+} and Bi^{3+} ions, a local expansion of the crystallographic site, as the "4.1 Analysis on structural properties" section describes, occurs in the $ScV_xP_{1-x}O_4:Bi^{3+}$. This local expansion amounts ≈ 6 % in $ScVO_4:Bi^{3+}$ [33], *i.e.*, <Bi-O> = 1.06 <Sc-O>, taking the <Sc-O> bond distances from **Table 3**. This value is assumed as indicatively representative of the average local site expansion of Bi-O bonds within the entire $ScV_xP_{1-x}O_4:Bi^{3+}$ system. Hence, we calculated the environmental factors $he_8(Bi)$ on this ground for all values of x in the solid solution. Values are given in **Table 4**. The corresponding $E_{A,8}(Bi)$ energies are then easily obtained by mean of equation 2. In case that an oxygen vacancy is present in the first neighborhood of Bi^{3+} ion, as identified earlier in $ScVO_4:Bi^{3+}$ [33], the coordination number of Bi^{3+} will be reduced to 7 with a resulting local expansion of the crystallographic site by ≈ 14 % with respect to virgin $ScVO_4$. We obtain $he_7(Bi)$ = 1.405 and $E_{A,8}(Bi)$ = 27880 cm^{-1} (359 nm) for this specific case.

The energy of D transitions in cm^{-1} (*i.e.*, Bi^{3+} -to-V^{5+} MMCT) can be estimated using [37]:

$$E_{D,CN}(Bi-V) = k_{CN'}^{CN}\left[\chi_{CN}(Bi^{3+}) - \alpha_{CN'}^{CN}\frac{\chi_{CN'}(V^{5+})}{d_{corr}}\right] \quad (3)$$

where $\chi_{CN}(Bi^{3+})$ and $\chi_{CN'}(V^{5+})$ are the electronegativities of Bi^{3+} and V^{5+} in CN and CN'-fold coordination, respectively, as calculated by Li *et al* [78]; for the specific purpose of the present work, we need $\chi_8(Bi^{3+})$ = 1.34 (*i.e.*, Bi^{3+} in regular eight-fold coordination) and $\chi_4(V^{5+})$ = 2.46 (*i.e.*, V^{5+} in tetrahedral coordination); d_{corr} is the shortest Bi^{3+}-V^{5+} interatomic distance corrected for the doping effect defined as $d_{corr} = d_{host} + 1/2\ \Delta r_{CN}$, where d_{host} is the shortest distance separating V^{5+} and Sc^{3+} cation sites in the undoped lattice (*i.e.*, the Sc-P/V distances given in **Table 3**). Here we have $\Delta r_8 = r_8(Bi^{3+}) - r_8(Sc^{3+})$, where $r_8(Bi^{3+})$ and $r_8(X)$ are the crystal radii of Bi^{3+} and Sc^{3+} in eight-fold coordination [68]. **Table 4** gives all d_{corr} values for all *x* values in $ScV_xP_{1-x}O_4:Bi^{3+}$. $k_{CN'}^{CN}$ and $\alpha_{CN'}^{CN}$ are the crystal-structure related quantities available from [37]. Here, we need $k_4^8 = 52239\ cm^{-1}$ and $\alpha_4^8 = 0.99$ for the calculation of all $E_{D,8}(Bi\text{-}V)$ energies by means of equation (3). At this stage, it should be kept in mind that the intensity of the Bi-V MMCT bands depends on the probability for a given Bi^{3+} ion to find a V^{5+} (or a $[VO_4]^{3-}$ unit) in its immediate neighborhood. This probability writes $P(x) = 1-(1-x)^n$, where *x* is the molar ratio in $ScV_xP_{1-x}O_4$ and *n* is the number of V^{5+} (P^{5+}) sites contained in the first coordination sphere of a given Bi^{3+}, *i.e.*, *n* = 2 in the zircon structure. All the values are given in **Table 4**. They give information on the probability of Bi-V MMCT transitions to occur in the $ScV_xP_{1-x}O_4:Bi^{3+}$ and therefore on the intensity of the transition. At last, we also provide in **Table 4** some available information on the host fundamental excitation (HFE) in virgin $ScV_xP_{1-x}O_4$ that depend on the <V-O> distances [78]. **Figure 4(d)** shows the variation of HFE, excitation tail, excitation edge, $E_{A,8}(Bi)$ and $E_{D,8}(Bi\text{-}V)$ against *x*. Meanwhile, energy $E_{A,7}(Bi)$ is also added for

the specific $ScVO_4:Bi^{3+}$ composition and $E_{A,8}(Sc)$ for $x \leq 0.2$.

We note that the host fundamental excitation (HFE) of virgin $ScV_xP_{1-x}O_4$ and energy position of excitation edge of $ScV_xP_{1-x}O_4:Bi^{3+}$ vary similarly with x. The energy downshift in the latter case is attributed to Bi^{3+} doping. The noticeable thing is the very peculiar behavior of $ScVO_4:Bi^{3+}$ that shows a pronounced redshift of its excitation edge, as pointed out already [33]. **Figure 4d** exhibits information on the energy level structure of Bi^{3+} in $ScV_xP_{1-x}O_4$. In this case, here we can confirm that D (Bi-V MMCT) and A transitions ($^1S_0$ - $^3P_1$) of Bi^{3+} have similar energy in such systems ($ScPO_4:Bi^{3+}$ excepted) [80]. The calculation locates a cross-over for x = 0.8, meaning that the lowest-lying excitation has an A character in $ScV_{0.9}P_{0.1}O_4:Bi^{3+}$ and $ScVO_4:Bi^{3+}$. In the latter case, the calculated energy $E_{A,7}(Bi)$ corresponding to an $^1S_0 - {}^3P_1$ transition of Bi^{3+} having an oxygen vacancy in its immediate neighborhood reproduces reasonably the spectacular redshift of the first derivative of excitation edge in this vanadate. Moving to the other side, the D band is predicted slightly below the A transition, but here it should be reminded that the probability for the Bi-V MMCT to occur drops as x is decreased. This is indicated in **Figure 4d** by the size of the spots that are drawn in proportion with probability $P(x)$. In other words, the D band becomes in practice too weak to be observed in the spectra for $x \leq 0.4$ and presumably the A transition dominates here. For x < 0.2, *i.e.*, in the phosphorous-rich systems, we observe a noticeable deviation between the experimental edge and the predicted $E_{A,8}(Bi)$ energies. This reveals that the 6% local site expansion of Bi-O bonds that has been considered for the calculation of $E_{A,8}(Bi)$ does not hold anymore, which may be due to the increasing stiffness of the lattice as the amount of $[PO_4]^{3-}$ units grows. To illustrate this point, we have calculated $E_{A,8}(Sc)$ energies without considering any local expansion of the crystal site (*i.e.*, as if we were considering virgin $ScV_xP_{1-x}O_4$). The values are plotted in **Figure 4d** and better corresponds to the excitation edge. Presumably, the A energies associated with Bi^{3+} in the phosphorous-riche members of solid solution are located between $E_{A,8}(Sc)$ and $E_{A,8}(Bi)$ extrema. Further work needs to be done here to clarify the situation. At last, we find that HFE (*i.e.*, the $[VO_4]^{3-}$ excitation) overlaps the A and D bands for $x > 0.4$ and can contribute to the excitation spectrum if the excitation energy is transferred to Bi^{3+} ion. Considering a doping rate of 2%, the probability that a $[VO_4]^{3-}$ group possesses a Bi^{3+} ion in its immediate neighborhood in $ScVO_4:Bi^{3+}$ is less than 4%, meaning that host sensitization of the Bi^{3+} luminescence needs energy migration among vanadate units prior the energy transfer to Bi^{3+}. Diluting the vanadates in the solid solution $ScV_xP_{1-x}O_4:Bi^{3+}$ makes this migration less and less probable as x decreases. This specific point has been examined by *G. Blasse* in the late 60's and was concluded that the critical concentration for energy migration in this system is $x \approx 0.25$ [79]. This means that we can expect a contribution of HFE in the excitation

spectra of $ScV_xP_{1-x}O_4:Bi^{3+}$ for $1 \leq x \leq \approx 0.25$. Excepting the two extreme members of the solid solution, we thus can ascribe the emission of $ScV_xP_{1-x}O_4:Bi^{3+}$ to thermalized A and D states giving ΔS shifts of ≈ 9000 to ≈ 12000 to cm^{-1}. The emission of $ScVO_4:Bi^{3+}$ is confirmed to have an A character, but the origin of the blue emission in $ScPO_4:Bi^{3+}$ is still unsure at this stage, especially if we compare with the isostructural $YPO_4:Bi^{3+}$ compound which regularly emits at 245 nm for an excitation at 230 nm [44] with a very small Stokes shift.

Looking in details, however, we find a low-lying excitation feature with low intensity in the 325 - 425 nm region, with a maximum at ≈ 365 nm that is responsible for the 8.7 % spectral overlap with the blue emission. This denotes the presence of an electronic state that could be responsible for the blue emission, with a Stokes shift of ≈ 5000 cm^{-1}. The nature of this state, however, is at the moment not fixed and, thus, needs a further study.

4.5 UV-triggered anti-counterfeiting and information protection application

A closer re-inspection into **Table 2** reveals that the excitation tails between the different solid solution are different from each other. For example, an excitation tail wavelength gap of 61 nm appears between $ScPO_4:Bi^{3+}$ (337 nm) and $ScV_{0.8}P_{0.2}O_4:Bi^{3+}$ (398 nm); there is a tail gap of 62 nm between $ScV_{0.6}P_{0.4}O_4:Bi^{3+}$ (*i.e.*, 365 nm) and $ScVO_4:Bi^{3+}$ (*i.e.*, 427 nm). Moreover, as **Figure 4a** depicts, by exciting with different wavelengths, different solid solutions show different emission positions and the FWHM values. Hence, the spectral properties of $ScV_xP_{1-x}O_4:Bi^{3+}$ solid solution appear very attractive for temporal data storage, information encryption, and anti-counterfeiting applications. As a proof of concept, we first have built a home-built setup consisting of a Hitachi F-7000 fluorescence spectrophotometer, a Lumenera camera (INFINITY1) and a high-resolution fiber optical spectrometer (FG4000) (**Figure 5a**). Then, various compositions of $ScV_xP_{1-x}O_4:Bi^{3+}$ solid solution, *i.e.*, $ScV_{0.2}P_{0.8}O_4:Bi^{3+}$ and $ScV_{0.8}P_{0.2}O_4:Bi^{3+}$ with a mass (denoted hereafter) ratio of 4:1 (**blend 1**), $ScV_{0.7}P_{0.3}O_4:Bi^{3+}$ and $ScV_{0.3}P_{0.7}O_4:Bi^{3+}$ with a ratio of 5:2 (**blend 2**), $ScV_{0.6}P_{0.4}O_4:Bi^{3+}$ and $ScVO_4:Bi^{3+}$ with a ratio of 3:5 (**blend 3**), and $ScV_{0.1}P_{0.9}O_4:Bi^{3+}$ and $ScVO_4:Bi^{3+}$ with a ratio of 7:2 (**blend 4**), were employed and deposited onto a piece of quartz glass (**Figure 5b**). After positioned the phosphors-covered quartz glass onto this home-built setup, we could captured the photographs and allowed the blended phosphors to have selective excitation wavelengths at the same time. It is shown in **Table 2** that the gap of excitation tails between the $ScV_{0.2}P_{0.8}O_4:Bi^{3+}$ and $ScV_{0.8}P_{0.2}O_4:Bi^{3+}$ is 52 nm, which is large enough to cover the beam width (~2 mm) and length (~4 mm) of UV excitation and thus can allow to having enough resolution to distinguish the emission colors of the two blended samples. More specifically, when the excitation wavelengths of 260 nm and 380 nm were used, temporal variation of emission colors is observable. In **Figure 5b** and **Figure**

5c, the former excitation wavelength can excite all blended phosphors, leading to the superimposed luminescence contribution of each phosphor in the blend that can be finely tuned by appropriate adjustment of the mass ratios. The latter wavelength, however, only selectively excites the phosphors that can show an excitation tail exceeding to this wavelength, *e.g.*, the solid solution of $ScV_xP_{1-x}O_4:Bi^{3+}$ with $x > 0.7$. Thus, exciting at 380 nm, such as in the blended $ScV_{0.2}P_{0.8}O_4:Bi^{3+}$ and $ScV_{0.8}P_{0.2}O_4:Bi^{3+}$ phosphors, pumps the color analogous to that of the $ScV_{0.2}P_{0.8}O_4:Bi^{3+}$ solid solution, while upon excitation at 260 nm enables giving rise to a color that differs in that of each $ScV_{0.2}P_{0.8}O_4:Bi^{3+}$ and $ScV_{0.8}P_{0.2}O_4:Bi^{3+}$ solid solution. Hence, **blend 1** enables featuring a temporal information encryption behavior, allowing to possessing the multiple UV light-converted anti-counterfeiting feature. **Figure 5d** gives the CIE chromaticity coordinates and related digital photos taken upon at different excitation wavelengths. When taken into account a variety of emission colors the $ScV_xP_{1-x}O_4:Bi^{3+}$ solid solution, a wide range of temporal colors, derived from any two or more types of the solid solution (*i.e.*., the examples shown in **Figure 5b** and **Figure 5c**), can be anticipated, and they enable covering the whole visible spectral region.

5. Conclusion and Outlook

In summary, a new type of full-color tunable $ScV_xP_{1-x}O_4:Bi^{3+}$ ($0 \leq x \leq 1$) solid solution with strong UV excitation intensity yet featured no significant excitation in the visible spectral region is reported in this work. We reveal that gradual substitution of P ions with larger V ions in the $ScV_xP_{1-x}O_4:Bi^{3+}$ solid solution induces a progressive shift the excitation edge from 295 nm to 385 nm, excitation tail from 340 nm to 425 nm, and corresponding emission maximum from 455 nm to 641 nm. The redshift of the excitation edge as the x value is increased in the $ScV_xP_{1-x}O_4:Bi^{3+}$ is well explained by considering the overlapping contribution of features having different origins, either intra-ionic A-type transitions or transitions with charge transfer character. Emission in these systems arises from the lower-lying excitation levels and shifts concomitantly with these levels with an almost constant Stokes shift. Moreover, blending the $ScV_xP_{1-x}O_4:Bi^{3+}$ ($0 \leq x \leq 1$) solid solution with adjusted mass ratios has been proved to be promising candidates for use in security and authenticity purposes, such as temporal information encryption and decryption and UV-converted anti-counterfeiting. This work not only have contributed a new type of Bi^{3+}-doped tunable member to the big family of solid solutions, but also progresses in the understanding of the intrinsic luminescence-structure relationships in $ScV_xP_{1-x}O_4:Bi^{3+}$ ($0 \leq x \leq 1$) solid solution. Thereby, we expect that this work could participate to the design and discovery of more Bi^{3+} doped tunable solid solutions that are able to address the visible re-absorption problem for feature solid-state lighting technology. Meanwhile, we expect that more RE and non-RE doped tunable solid solutions and

relevant new application possibilities based upon their spectral features can be discovered through modulating the secondary cations in the isostructural crystals.

Acknowledgement

Here, we would like to acknowledge the financial supports from the Innovation and Technology Commission of HKSAR through Hong Kong Branch of National Precious Metals Material Engineering Research Center, City University of Hong Kong (Projects no. 9667143, and 7004902), and the European Union's Horizon 2020 research and innovation program under the Marie Sklodowska-Curie grant agreement no. 713683.

Table 1 Summarization on electronic bandgap (E_g) values of bulk $ScPO_4$ and $ScVO_4$ crystals. Noted that the theoretical E_g values highlighted by *a* contain $2H_2O$, while those denoted by *b* are

based upon using a GGA + *U* extension method. As the experimental E_g value highlighted by *c*, it is achieved using the *Urbach* rule's approximation method.

$ScPO_4$		*Refs.*	$ScVO_4$		*Refs.*
Exptl E_g /eV	*Calcd* E_g /eV	----	*Exptl* E_g /eV	*Calcd* E_g /eV	---
7.2	---	[57]	2.8	2.70 (GGA)[b]	[33]
---	4.52 (GGA)	[58]	2.8	2.75 (GGA)[b]	[62]
---	5.07 (LDA)	[59][a]	---	2.57 (GGA)	[63]
---	4.60 (LDA)	[60][a]	---	2.56 (GGA)	[64]
7.73[c]	---	[65]	---	2.48 (GGA)	[66]
6.73	4.11 (GGA)	*Here*	---	2.56 (GGA)[b]	*Here*

GGA --- Generalized Gradient Approximation LDA --- Local density approximation

Table 2 XRD position of planes spacing (112) and corresponding calculated *d* values of the $Sc(V_x,P_{1-x})O_4:Bi^{3+}$ ($0 \leq x \leq 1$) solid solution. Besides, experimental and fitted emission positions as well as emission fwhm values and excitation tails of the solid solution are also included here.

x	(112) /°	*d* /Å	λ_{em} peak /nm	Fitted λ_{em} /nm	FWHM /cm^{-1}	λ_{ex} tail /nm
0.0	36.536	2.4575	440	441.84	6240	337
0.1	36.353	2.4693	446	447.68	5680	338
0.2	36.143	2.4832	456	457.68	5780	346
0.3	35.910	2.4988	476	470.43	5820	355
0.4	35.772	2.5080	486	486.61	5790	359
0.5	35.512	2.5259	507	507.55	6250	360
0.6	35.429	2.5316	529	530.86	6120	365
0.7	35.177	2.5491	552	555.80	6690	368
0.8	35.012	2.5607	591	574.14	7050	390
0.9	34.891	2.5694	614	613.90	6985	398
1.0	34.671	2.5849	640	642.14	5730	427

Table 3 Rietveld refined XRD results for the $Sc(V_x,P_{1-x})O_4:Bi^{3+}$ ($0 \leq x \leq 1$) solid solution.

x	$a(b)$/Å	c/Å	V/Å^3	<*Sc-O*>/Å	Sc-P/V/Å	<*V-O*>/Å	R_p/%	R_{wp}/%	R_{exp}/%	R_{Bragg}/%	R_F/%	GOF
0.0	6.5741	5.7918	250.32	2.2490	2.8958	---	14.5	13.4	9.67	2.634	1.867	1.91
0.1	6.5905	5.8192	252.75	2.2174	2.9095	1.5376	15.6	14.0	10.38	1.955	1.682	1.83
0.2	6.6055	5.8469	255.12	2.2246	2.9234	1.5427	20.1	16.7	11.34	5.519	3.756	2.16
0.3	6.6290	5.8871	258.70	2.2355	2.9436	1.5502	18.6	16.1	12.14	2.912	4.130	2.64
0.4	6.6534	5.9267	262.36	2.2465	2.9634	1.5578	17.0	14.4	10.71	3.088	2.157	1.82
0.5	6.6710	5.9586	265.17	2.2548	2.9793	1.5636	20.3	16.7	11.27	3.180	3.105	2.19
0.6	6.6945	5.9981	268.81	2.2656	2.9990	1.5711	18.6	14.3	11.60	3.000	3.088	1.51
0.7	6.7153	6.0283	271.85	2.2744	3.0142	1.5772	19.3	13.5	1.48	2.778	2.648	1.39
0.8	6.7371	6.0698	275.50	2.2851	3.0349	1.5847	21.8	17.1	11.70	3.349	2.484	2.13
0.9	6.7580	6.1019	278.68	2.2942	3.0509	1.5910	22.6	16.1	12.14	2.985	2.121	2.14
1.0	6.7787	6.1336	281.85	2.3032	3.0668	1.5973	19.1	13.0	11.47	2.785	2.662	1.28

Noted that the abbreviations of R_p, R_{wp}, R_{exp}, R_{Bragg} and R_F denote Profile factor, Weighted profile, factor Expected weighted profile factor, Bragg factor, and Crystallographic factor, respectively.

Table 4 Corrected Bi-V distances, environmental factor and spectral properties of Bi^{3+} in the $ScV_xP_{1-x}O_4$ solid solution

x	d_{corr} /Å	P (x)	he_8 (Bi)	HFE /cm^{-1}	Edge /cm^{-1}	ΔS /cm^{-1}	Crossing point /nm	Spectral overlap /%
0.0	3.0458	0	1.125	---	33900	11220	348	8.70
0.05	---	---	---	36800	---	---	---	---
0.1	3.0595	0.19	1.135	---	31645	9225	338	0.19
0.2	3.0734	0.36	1.137	34500	30490	8655	345	0.17
0.3	3.0936	0.51	1.143	---	30210	9200	354	0.22
0.4	3.1134	0.64	1.149	31600	29585	9000	356	0.27
0.5	3.1293	0.75	1.152	---	29585	9900	357	0.19
0.6	3.1490	0.84	1.157	---	29070	10165	369	0.59
0.7	3.1642	0.91	1.161	---	29154	10740	372	0.44[a]
0.75	---	---	---	30600	---	---	---	---
0.8	3.1849	0.96	1.166	---	28820	11900	384	0.42
0.9	3.2009	0.99	1.170	---	28570	12285	386	0.63
1.0	3.2168	1	1.173	29800	26040	10440	416	2.41

Figure captions

Figure 1 (**a**) Calculated density of state (DOS) of $Sc(V_x,P_{1-x})O_4$ (x = 0, 0.25, 0.50, 0.75, 1.00), where the E_g values are also given; (**b**) Crystal structure of intermediate $Sc(V_x,P_{1-x})O_4$ (x = 0.50) compound; (**c**) Lattice cells of $ScPO_4$ (*i.e.*, from ICSD file no. 74483) and $ScVO_4$ (*i.e.*, from ICSD file no. 78074) as well as the cationic coordination environments and schematic illustration of the substitution process that involves the substitution of the Sc site with the Bi dopant and the P atom with the V atom. The Sc-O and P-O lengths in the $ScPO_4$ lattice, along with the Sc-O and V-O lengths in the $ScVO_4$ lattice are also given in **Figure 1c**.

Figure 2 XRD patterns of $Sc(V_x,P_{1-x})O_4:Bi^{3+}$ ($0 \leq x \leq 1$) solid solution and the corresponding enlarged diffraction patterns within the range of 34-37°.

Figure 3 Refined XRD patterns (−) of $ScPO_4:Bi^{3+}$ (**a**) and $Sc(V_{0.5},P_{0.5})O_4:Bi^{3+}$ (**b**) compounds, where the Rietveld refining results, Bragg reflections, profile differences between experimental and calculated values are denoted using the ×, | and – symbols, respectively; (**c**), (**d**) and (**e**) are the x-dependent cell lattice parameters *a*/*b*, *c* and *V*, where the linear fitting are based upon the equation of $y = m + nx$.

Figure 4 (**a**) Excitation and emission spectra of the $Sc(V_x,P_{1-x})O_4:Bi^{3+}$ ($0 \leq x \leq 1$) solid solution, all spectra are normalized to unity; (**b**) CIE chromaticity coordinates calculated using the emission of (**a**), the cross points of the excitation and the emission spectra, along with the emission wavelengths used for monitoring the excitation spectra, are also denoted beside each excitation curve; (**c**) Energy level structure of Bi^{3+} in $ScV_xP_{1-x}O_4$, where (**i**) is the host fundamental excitation (HFE), excitation edge and tail, (**ii**) is the calculated position of A and D transitions.

Figure 5 (**a**) Home-built PL setup of how to collect the digital photos (**b**) and emission spectra (**c**) of the blended phosphors upon excitation at different wavelengths, as well as the related CIE values (**d**). In (**b-c**), the blended phosphors are $ScV_{0.2}P_{0.8}O_4:Bi^{3+}$ and $ScV_{0.8}P_{0.2}O_4:Bi^{3+}$ with a mass (denoted hereafter) ratio of 4:1 (**blend 1**, **points 1-2**), $ScV_{0.7}P_{0.3}O_4:Bi^{3+}$ and $ScV_{0.3}P_{0.7}O_4:Bi^{3+}$ with a ratio of 5:2 (**blend 2**, **point 3**), $ScV_{0.6}P_{0.4}O_4:Bi^{3+}$ and $ScVO_4:Bi^{3+}$ with a ratio of 3:5 (**blend 3**, **point 4**), and $ScV_{0.1}P_{0.9}O_4:Bi^{3+}$ and $ScVO_4:Bi^{3+}$ with a ratio of 7:2 (**blend 4**, **point 5**). The excitation wavelengths and the corresponding CIE values have been also labeled besides each curve and/or suitable place.

References

(1) Xing, G. C.; Mathews, N.; Lim, S. S.; Yantara, N.; Liu, X. F.; Sabba, D.; Grätzel, M.; Mhaisalkar, S.; Sum, T. C. "Low-temperature solution-processed wavelength-tunable perovskites for lasing." ***Nat. Mater.***, 2014, *13*, 476-480.

(2) Xie, W.; Mo, Y. M.; Zou, C. W.; Kang, F. W.; Sun, G. H. "Broad color tuning and Eu^{3+}-related photoemission enhancement via controllable energy transfer in the $La_2MgGeO_6:Eu^{3+},Bi^{3+}$ phosphor." *Inorg. Chem. Front.*, **2018**, *5*, 1076-1084.

(3) Dai, P. P.; Li, C.; Zhang, X. T.; Xu, J.; Chen, X.; Wang, X. L.; Jia, Y.; Wang, X. J.; Liu, Y. -C. "A single Eu^{2+}-activated high-color-rendering oxychloride white-light phosphor for white-light-emitting diodes. ***Light Sci. Appl.***, 2016, *5*, e16024.

(4) Chang, C.-K.; Chen, T. -M. "White light generation under violet-blue excitation from tunable green-to-red emitting $Ca_2MgSi_2O_7$:Eu,Mn through energy transfer." ***Appl. Phys. Lett.***, 2007, *90*, 161901.

(5) Kimura, N.; Sakuma, K.; Hirafune, S.; Asano, K.; Hirosaki, N.; Xie, R. -J. "Extrahigh color rendering white light-emitting diode lamps using oxynitride and nitride phosphors excited by blue light-emitting diode." ***Appl. Phys. Lett.***, 2007, *90*, 051109.

(6) Wang, L.; Xie, R. J.; Li, Q.; Wang, J.; Ma, G.; Luo, D.; Takeda, T.; Tsai, Y. T.; Liu, R.S.; Hirosaki, N. "$Ca_{1-x}Li_xAl_{1-x}Si_{1+x}N_3:Eu^{2+}$ solid solutions as broadband, color-tunable and thermally robust red phosphors for superior color rendition white light-emitting diodes." ***Light Sci. Appl.***, 2016, *5*, e16155.

(7) Im, W. B.; George, N.; Kurzman, J.; Brinkley, S.; Mikhailovsky, A.; Hu, J.; Chmelka, B. F.; DenBaars, S. P.; Seshadri, R. "Efficient and Color-Tunable Oxyfluoride Solid Solution Phosphors for Solid-State White Lighting." ***Adv. Mater.***, 2011, *23*, 2300-2305.

(8) Zhang, S. Y.; Huang, Y. L.; Kai, W. F.; Shi, L.; Seo, H. J. "Tunable Red Luminescence of Mn^{2+}-Doped $NaCaPO_4$ Phosphors." ***Electrochem. Solid-State Lett.***, 2010, *13*, J11-J14.

(9) Akihiko, K., Satoshi, H. "H_2 or O_2 Evolution from Aqueous Solutions on Layered Oxide Photocatalysts Consisting of Bi^{3+} with $6s^2$ Configuration and d^0 Transition Metal Ions." ***Chem. Lett.***, 1999, *28*, 1103-1104.

(10) Ju, G. F.; Hu, Y. H.; Chen, L.; Wang, X. J.; Mu, Z. F.; Wu, H. Y.; Kang, F. W. "Luminescent properties of $Na_3Gd_{1-x}Eu_x(PO_4)_2$ and energy transfer in these phosphors." ***J. Alloy Compd.***, 2011, *509*, 5655-5659.

(11) Wong, E. Y. "Configuration Interaction of the Pr^{3+} Ion." ***J. Chem. Phys.***, 1963, *38*, 976-978.

(12) Wu, H. Y.; Hu, Y. H.; Kang, F. W.; Chen, L.; Wang, X. J.; Ju, G. F.; Mu, Z. F. "Observation on long afterglow of Tb^{3+} in $CaWO_4$." ***Mater. Res. Bull.***, 2011, *46*, 2489-2493.

(13) Foster, D. R.; Reid, M. F.; Richardson, F. S. "Optical emission spectra and crystal-field analysis of Tm^{3+} in the cubic Cs_2NaYCl_6 host." ***J. Chem. Phys***., 1985, *83*, 3225-3233.

(14) Carnall, W. T.; Fields, P. R.; Rajnak, K. "Electronic Energy Levels in the Trivalent Lanthanide Aquo Ions. I. Pr^{3+}, Nd^{3+}, Pm^{3+}, Sm^{3}+, Dy^{3+}, Ho^{3+}, Er^{3+}, and Tm^{3+}." ***J. Chem. Phys.***, 1968, *49*, 4424-4442.

(15) Kang, F. W.; He, J. J.; Sun, T. Y.; Bao, Z. Y.; Wang, F.; Lei, D. Y. "Plasmonic Dual-Enhancement and Precise Color Tuning of Gold Nanorod@SiO_2 Coupled Core-Shell-Shell Upconversion Nanocrystals." ***Adv. Funct. Mater.***, 2017, *27*, 1701842.

(16) Brik, M. G.; Srivastava, A. M. "On the optical properties of the Mn^{4+} ion in solids." ***J. Lumin.***, 2013, *133*, 69-72.

(17) Wood, D. L.; Ferguson, J.; Knox, K.; Dillon Jr. J. F. "Crystal-Field Spectra of $d^{3,7}$ Ions. III. Spectrum of Cr^{3+} in Various Octahedral Crystal Fields." ***J. Chem. Phys.***, 1963, *39*, 890-898.

(18) Chen, M.; Xia, Z.; Molokeev, M. S.; Liu, Q. "Structural Phase Transformation and Luminescent Properties of $Ca_{2-x}Sr_xSiO_4:Ce^{3+}$ Orthosilicate Phosphors. ***Inorg. Chem.***, 2015, *54*, 11369-11376.

(19) Ji, X. Y.; Zhang, J. L.; Li, Y.; Liao, S. Z.; Zhang, X. G.; Yang, Z. Y.; Wang, Z. L.; Qiu, Z. X.; Zhou, W. L.; Yu, L. P.; Lian, S. X. "Improving Quantum Efficiency and Thermal Stability in Blue-Emitting $Ba_{2-x}Sr_xSiO_4:Ce^{3+}$ Phosphor via Solid Solution." ***Chem. Mater.***, 2018, *30*, 5137-5147.

(20) Dai, P. P.; Zhang, X. T.; Bian, L. L.; Lu, S.; Liu, Y. C.; Wang, X. J. "Color tuning of $(K_{1-x},Na_x)SrPO_4:0.005Eu^{2+},yTb^{3+}$ blue-emitting phosphors via crystal field modulation and energy transfer." ***J. Mater. Chem. C***, 2013, *1*, 4570-4576.

(21) Zhang, X. G.; Xu, J. G.; Guo, Z. Y.; Gong, M. L. "Luminescence and energy transfer of dual-emitting solid wolution phosphors $(Ca,Sr)_{10}Li(PO_4)_7:Ce^{3+},Mn^{2+}$ for ratiometric temperature sensing." ***Ind. Eng. Chem. Res.***, 2017, *56*, 890-898.

(22) Kang, F. W.; Peng, M. Y.; Yang, X. B.; Dong, G. P.; Nie, G. C.; Liang, W. J.; Xu, S. H.; Qiu, J. R. "Broadly tuning Bi^{3+} emission via crystal field modulation in solid solution compounds $(Y,Lu,Sc)VO_4$:Bi for ultraviolet converted white LEDs." ***J. Mater. Chem. C***, 2014, *2*, 6068-6076.

(23) Xia, Z. G.; Liu, G. K.; Wen, J. G.; Mei, Z. G.; Balasubramanian, M.; Molokeev, M. S.; Peng, L. C.; Gu, J.; Miller, D. J.; Liu, Q. L.; Poeppelmeier, K. R. "Tuning of Photoluminescence by Cation

Nanosegregation in the $(CaMg)_x(NaSc)_{1-x}Si_2O_6$ Solid Solution." ***J. Am. Chem. Soc.***, 2016, *138*, 1158.

(24) Xiao, W. G.; Wu, D.; Zhang, L. L.; Zhang, X.; Hao, Z. D.; Pan, G. H.; Zhang, L. G.; Ba, X. W.; Zhang, J. H. "The Inductive Effect of Neighboring Cations in Tuning Luminescence Properties of the Solid Solution Phosphors." ***Inorg. Chem.***, 2017, *56*, 9938-9945.

(25) Trotochaud, L.; Boettcher, S. W. "Synthesis of Rutile-Phase $Sn_xTi_{1-x}O_2$ Solid-Solution and $(SnO_2)_x/(TiO_2)_{1-x}$ Core/Shell Nanoparticles with Tunable Lattice Constants and Controlled Morphologies." ***Chem. Mater.***, 2011, *23*, 4920-4930.

(26) Chen, H.; Ding, J. Y.; Ding, X.; Wang, X. C.; Cao, Y. X.; Zhao, Z. Y.; Wang, Y. H. "Synthesis, Crystal Structure, and Luminescence Properties of Tunable Red-Emitting Nitride Solid Solutions $(Ca_{1-x}Sr_x)_{16}Si_{17}N_{34}:Eu^{2+}$ for White LEDs." ***Inorg. Chem.***, 2017, *56*, 10904-10913.

(27) Ji, H. P.; Huang, Z. H.; Xia, Z. G.; Molokeev, M. S.; Atuchin, V. V.; Huang, S. F. "Cation Substitution Dependent Bimodal Photoluminescence in Whitlockite Structural $Ca_{3-x}Sr_x(PO_4)_2:Eu^{2+}$ ($0 \leq x \leq 2$) Solid Solution Phosphors." ***Inorg. Chem.***, 2014, *53*, 11119-11124.

(28) Kim, J. S.; Park, Y. H.; Choi, J. C.; Park, H. L. "Optical and Structural Properties of Eu^{2+}-doped $(Sr_{1-x}Ba_x)_2SiO_4$ phosphors." ***J. Electrochem. Soc.***, 2005, *152*, H135-H137.

(29) Tang, W. J.; Xue, H. J. "Preparation of $Sr_8Mg_{1-m}Zn_mY(PO_4)_7:Eu^{2+}$ solid solutions and their luminescence properties." ***RSC Adv.***, 2014, *4*, 62230-62236.

(30) Shang, M. M.; Li, C. X.; Lin, J. "How to produce white light in a single-phase host***?" Chem. Soc. Rev.***, 2014, *43*, 1372-1386.

(31) Jalalah, M.; Ko, Y. H.; Harraz, F. A.; Al-Assiri, M. S.; Park, J. G. "Enhanced efficiency and current density of solar cells via energy-down-shift having energy-tuning-effect of highly UV-light-harvesting Mn^{2+}-doped quantum dots." ***Nano Energy***, 2017, *33*, 257-265.

(32) Han, J.; Li, L. J.; Peng, M. Y.; Huang, B. L.; Pan, F. J.; Kang, F. W.; Li, L. Y.; Wang, J.; Lei, B. F. "Toward Bi^{3+} Red Luminescence with No Visible Reabsorption through Manageable Energy Interaction and Crystal Defect Modulation in Single Bi^{3+}-Doped $ZnWO_4$ Crystal." ***Chem. Mater.***, 2017, *29*, 8412-8424.

(33) Kang, F. W.; Yang, X. B.; Peng, M. Y.; Wondraczek, L.; Ma, Z. J.; Zhang, Q. Y.; Qiu, J. R. "Red Photoluminescence from Bi^{3+} and the Influence of the Oxygen-Vacancy Perturbation in $ScVO_4$: A Combined Experimental and Theoretical Study." ***J. Phys. Chem. C***, 2014, *118*, 7515-7522.

(34) Müller, M.; Jüstel, T. “Energy transfer and unusual decay behavior of $BaCa_2Si_3O_9:Eu^{2+},Mn^{2+}$ phosphor.” ***Dalton Trans.***, 2015, *44*, 10368-10376.

(35) Wei, Y.; Xing, G. C.; Liu, K.; Li, G. G.; Dang, P. P.; Liang, S. S.; Liu, M.; Cheng, Y.; Jin, Y.; Lin, J. “New strategy for designing orangish-red emitting phosphor via oxygen-vacancy induced electronic localization.” ***Light-Sci. Appl.***, 2019, *8*, 15.

(36) Kang, F. W.; Zhang, H. S.; Wondraczek, L.; Yang, X. B.; Zhang, Y.; Lei, D. Y.; Peng, M. Y. “Band-Gap Modulation in Single Bi^{3+}-Doped Yttrium-Scandium-Niobium Vanadates for Color Tuning over the Whole Visible Spectrum.” ***Chem. Mater.***, 2016, *28*, 2692-2703.

(37) Boutinaud, P. “Revisiting the Spectroscopy of the Bi^{3+} Ion in Oxide Compounds.” ***Inorg. Chem.***, 2013, *52*, 6028-6038.

(38) Kang, F. W.; Peng, M. Y.; Lei, D. Y.; Zhang, Q. Y. “Recoverable and Unrecoverable Bi^{3+}-Related Photoemissions Induced by Thermal Expansion and Contraction in $LuVO_4:Bi^{3+}$ and $ScVO_4:Bi^{3+}$ Compounds.” ***Chem. Mater.***, 2016, *28*, 7807-7815.

(39) Wolfert, A.; Oomen, L.; Blasse, G. “Host lattice dependence of the Bi^{3+} luminescence in orthoborates $LnBO_3$ (with Ln = Sc, Y, La, Gd, or Lu).” ***J. Solid State Chem.***, 1985, *59*, 280-290.

(40) Li, X.; Li, P. L.; Wang, Z. J.; Liu, S. M.; Bao, Q.; Meng, X. Y.; Qiu, K. L.; Li, Y. B.; Li, Z. Q.; Yang, Z. P. “Color-Tunable Luminescence Properties of Bi^{3+} in $Ca_5(BO_3)_3F$ via Changing Site Occupation and Energy Transfer.” ***Chem. Mater.***, 2017, *29*, 8792-8803.

(41) Kang, F. W.; Peng, M. Y.; Zhang, Q. Y.; Qiu, J. R. “Abnormal Anti-Quenching and Controllable Multi-Transitions of Bi^{3+} Luminescence by Temperature in a Yellow-Emitting $LuVO_4:Bi^{3+}$ Phosphor for UV-Converted White LEDs.” ***Chem. Eur. J.***, 2014, *20*, 11522-11530.

(42) Li, H. M.; Pang, R.; Liu, G. Y.; Sun, W. Z.; Li, D.; Jiang, L. H.; Zhang, S.; Li, C. Y.; Feng, J.; Zhang, H. J. “Synthesis and Luminescence Properties of Bi^{3+}-Activated K_2MgGeO_4: A Promising High-Brightness Orange-Emitting Phosphor for WLEDs Conversion.” ***Inorg. Chem.***, 2018, *57*, 12303-12311.

(43) Dang, P. P.; Liang, S. S.; Li, G. G.; Lian, H. Z.; Shang, M. M.; Lin, J. “Broad color tuning of Bi^{3+}/Eu^{3+}-doped $(Ba,Sr)_3Sc_4O_9$ solid solution compounds via crystal field modulation and energy transfer.” ***J. Mater. Chem. C***, 2018, *6*, 9990-9999.

(44) Cavalli, E.; Angiuli, F.; Mezzadri, F.; Trevisani, M.; Bettinelli, M.; Boutinaud, P.; Brik, M. G. “Tunable luminescence of Bi^{3+}-doped $YP_xV_{1-x}O_4$ ($0 \leq x \leq 1$).” ***J. Phys.: Condens. Matter.***, 2014, *26*, 385503.

(45) Chen, L.; Zhang, Y.; Luo, A. Q.; Liu, F. Y.; Jiang, Y.; Hu, Q. Z.; Chen, S. G.; Liu, R.-S. "The temperature-sensitive luminescence of (Y,Gd)VO_4:Bi^{3+},Eu^{3+} and its application for stealth anti-counterfeiting." ***Phys. Status Solidi RRL***, 2012, *6*, 321-323.

(46) Chen, L.; Chen, K. J.; Hu, S. F.; Liu, R. S. Combinatorial Chemistry Approach to Searching Phosphors for White Light-Emitting Diodes in (Gd-Y-Bi-Eu)VO_4 Quaternary System. *J. Mater. Chem.* **2011**, *21*, 3677-3685.

(47) Tian, S. Y.; Zhao, L.; Chen, W. B.; Liu, Z. C.; Fan, X. T.; Min, Q. H.; Yu, H.; Yu, X.; Qiu, J. B.; Xu, X. H. "Abnormal photo-stimulated luminescence in $Ba_2Ga_2GeO_7$:Tb^{3+}, Bi^{3+}." ***J. Lumin.***, 2018, *202*, 414-419.

(48) Hazra, C.; Sarkara, S.; Mahalingam, V. "Selective reduction of visible upconversion emissions induced by Bi^{3+} in Tm^{3+}/Yb^{3+}-doped $Y_{0.89-x}Bi_xVO_4$ microcrystals." ***RSC Adv.***, 2012, *2*, 6926-6931.

(49) Huang, Q. Y.; Ye, W. H.; Hu, G. Q.; Liu, X. T. "Strong red emission in Bi^{3+} and Mn^{4+} codoped $Mg_{3.5}Ge_{1.25}O_6$ phosphors applied in optical agriculture." ***J. Lumin.***, 2019, 210, 89-95.

(50) Zhou, Z.; Zhong, Y.; Xia, M.; Zhou, N.; Lei, B. F.; Wang, J.; Wu, F. F. "Tunable dual emission of $Ca_3Al_4ZnO_{10}$:Bi^{3+},Mn^{4+} via energy transfer for indoor plant growth lighting." ***J. Mater. Chem. C***, 2018, *6*, 8914-8922.

(51) Sandhyarani, A.; Kokila, M. K.; Darshan, G. P.; Basavaraj, R. B.; Prasad, B. D.; Sharma, S. C.; Lakshmi, T. K. S.; Nagabhushana, H. "Versatile core–shell SiO_2@$SrTiO_3$:Eu^{3+}, Li^+ nanopowders as fluorescent label for the visualization of latent fingerprints and anti-counterfeiting applications." ***Chem. Eng. J.***, 2017, *327*, 1135-1150.

(52) Marappa, B.; Rudresh, M. S.; Basavaraj, R. B.; Darshan, G. P.; Prasad, B. D.; Sharma, S. C.; Sivakumari, S.; Amudh P.; Nagabhushana, H. "EGCG assisted Y_2O_3:Eu^{3+} nanopowders with 3D micro-architecture assemblies useful for latent finger print recognition and anti-counterfeiting applications." ***Sensor Actuat B-Chem.***, 2018, *264*, 426-439.

(53) Kang, F. W.; Sun, G. H.; Wang, A. W.; Xiao, X. F.; Li, Y. Y.; Lu, J.; Huang, B. L. "Multicolor Tuning and Temperature-Triggered Anomalous Eu^{3+}-Related Photoemission Enhancement via Interplay of Accelerated Energy Transfer and Release of Defect-Trapped Electrons in the Tb^{3+},Eu^{3+}-Doped Strontium-Aluminum Chlorites." ***ACS Appl. Mater. Interfaces***, 2018, *10*, 36157-36170.

(54) Kresse, G.; Furthmüller, J. "Efficient iterative schemes for ab initio total-energy calculations using a plane-wave basis set." ***Phys. Rev. B***, 1996, *54*, 11169-11186.

(55) Kresse, G.; Furthmüller, J. “From ultrasoft pseudopotentials to the projector augmented-wave method.” ***Phys. Rev. B***, 1999, *59*, 1758-1775.

(56) Blöchl, P. E. “Projector augmented-wave method.” ***Phys. Rev. B***, 1994, *50*, 17953-17979.

(57) Trukhin A.; Boatner L. A. “Electronic structure of $ScPO_4$ single crystals: Optical and photoelectric properties.” ***Mater. Sci. Forum***, 1997, *239-241*, 573-576.

(58) Kristin, P. “Materials Data on $ScPO_4$ (SG:141) by Materials Project.” United States: N. p., 2014, // doi:10.17188/1207954.

(59) Xu, H. L.; Xu, B.; Liu, R.; Li, X. W.; Zhang, S. Q.; Ouyang, C. Y.; Zhong, S. L. “Facile microwave synthesis of $ScPO_4{\cdot}2H_2O$ flowerlike superstructures: morphology control, electronic structure and multicolor tunable luminescent properties.” ***CrystEngComm***, 2017, *19*, 5787-5796.

(60) Singh, D. J.; Jellison, G. E.; Jr., Boatner, L. A. “Electronic structure of Pb- and non-Pb-based phosphate scintillators.” ***Phys. Rev. B***, 2006, *74*, 155126.

(61) Krumpel, A. H.; Boutinaud, P.; va der Kolk, E.; Dorenbos, P. “Charge transfer transitions in the transition metal oxides ABO_4:Ln^{3+} and APO_4:ln^{3+} (A = La, Gd, Y, Lu, Sc; B=V, Nb, Ta; Ln = lanthanide).” ***J. Lumin.***, 2010, *130*, 1357-1365.

(62) Garg, A. B.; Errandonea, D.; Rodríguez, H. P.; Muñoz, A. “$ScVO_4$ under non-hydrostatic compression: a new metastable polymorph.” ***J. Phys.: Condens. Matter.***, 2017, *29*, 055401.

(63) Cong, H. J.; Zhang, H. J.; Yao, B.; Yu, W. T.; Zhao, X.; Wang, J. Y.; Zhang, G. C. “$ScVO_4$: Explorations of Novel Crystalline Inorganic Optical Materials in Rare-Earth Orthovanadate Systems.” ***CrystEngComm***, 2010, *10*, 4389-4400.

(64) Shwetha, G.; Kanchana V.; Vaitheeswaran G. “Optical properties of orthovanadates, and periodates studied from first principles theory.” ***Matter. Chem. Phys.***, 2015, *163*, 376-386.

(65) A.N. Trukhin, L.A. Boatner, Luminescence properties of $ScPO_4$ single crystals, in: V. Michailin (Ed.), ***Proceeding of the 5th International Conference on Inorganic Scintillators and their Applications***, University of Moscow, Moscow, Russia, 2000, 697-702.

(66) Wei, X. T.; Wen, J.; Li, S.; Huang, S.; Cheng, J.; Chen, Y. H.; Duan, C. K.; Yin, M. “Red-shift of vanadate band-gap by cation substitution for application in phosphor-converted white light-emitting diodes.” ***Appl. Phys. Lett.***, 2014, *104*, 181904.

(67) Kang, F. W.; Li, L. J.; Han, J.; Lei, D. Y.; Peng, M. Y. “Emission color tuning through manipulating the energy transfer from VO_4^{3-} to Eu^{3+} in single-phased $LuVO_4$:Eu^{3+} phosphors.” ***J. Mater. Chem. C***, 2017, *5*, 390-398.

(68) Shannon, R. D. “Revised Effective Ionic Radii and Systematic Studies of Interatomic Distances in Halides and Chalcogenides,” ***Acta Crystallographica***, 1976, *A32*, 751-767.

(69) Ahrens, L. H. “The use of ionization potentials Part 1. Ionic radii of the elements**,” *Geochim. Cosmochim. Acta***, 1952, *2*, 155-169.

(70) Roy, H. P. A.; Pieter, D. “The Bi^{3+} 6*s* and 6*p* electron binding energies in relation to the chemical environment of inorganic compounds.” ***J. Lumin.***, 2017, *184*, 221-231.

(71) Boutinaud, P. “On the luminescence of Bi^{3+} pairs in oxidic compounds.” ***J. Lumin.***, 2018, 197, 228-232.

(72) Wang, L. L.; Sun, Q.; Liu, Q. Z.; Shi, J. S. “Investigation and application of quantitative relationship between *sp* energy levels of Bi^{3+} ion and host lattice.” ***J. Solid State Chem.***, 2012, *191*, 142-146.

(73) Shi, J. S.; Wu, Z. J.; Zhou, S. H.; Zhang, S. Y. “Dependence of crystal field splitting of 5*d* levels on hosts in the halide crystals.” ***Chem. Phys. Lett.***, 2003, *380*, 245-250.

(74) Shi, J. S.; Zhang, S. Y. “Barycenter of Energy of Lanthanide $4f^{N-1}5d$ Configuration in Inorganic Crystals.” ***J. Phys. Chem. B****,* 2004, *108*, 18845-18849.

(75) Amer, M.; Boutinaud, P. “The doping sites in Eu^{2+}-doped $A^{I}B^{II}PO_4$ phosphors and their consequence on the photoluminescence excitation spectra.” ***J. Solid State Chem.***, 2018, *258*, 124-130.

(76) Momma, K.; Izumi, F. “VESTA: A Three-dimensional Visualization System for Electronic and Structural Analysis.” ***J. Appl. Crystallogr.***, 2008, *41*, 653-658.

(77) Brese, N. E.; O’Keefe, M. “Bond valence parameters for solids.” ***Acta Cryst.***, 1991, *B47*, 192-197.

(78) Li, K.; Xue, D. “Estimation of electronegativity values of elements in different valence states.” ***J. Phys. Chem. A***, 2006, *110*, 11332-11337.

(79) Blasse, G. “Some considerations and experiments on concentration quenching of characteristic broad-band fluorescence.” ***Philips Res. Repts.***, 1968, *23*, 344-361.

(80) Amer, M.; Boutinaud, P. “On the character of the optical transitions in closed-shell transition metal oxides doped with Bi^{3+}.” ***Phys. Chem. Chem. Phys.***, 2017, *19*, 2591-2596.

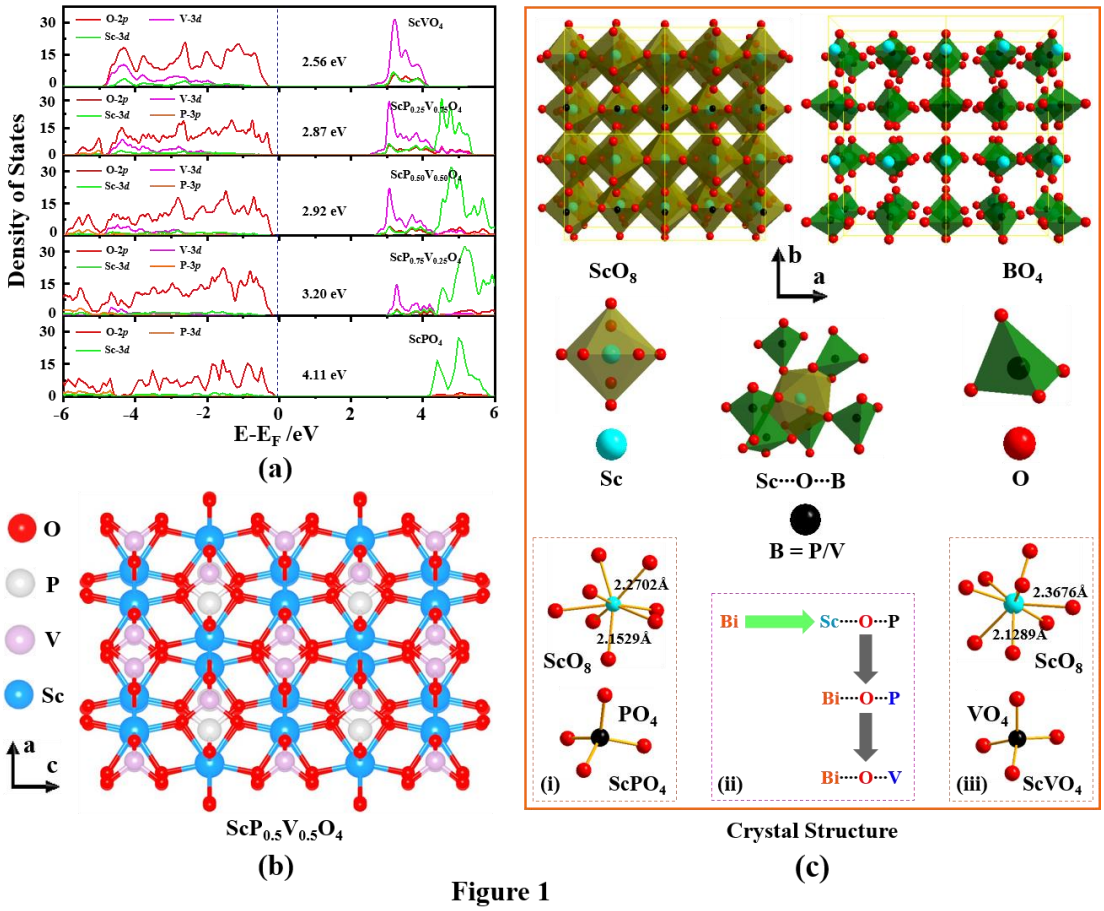
Density of States
O-2p
V-3d
Sc-3d
P-3p
P-3d
ScVO4
ScP0.25V0.75O4
ScP0.50V0.50O4
ScP0.75V0.25O4
ScPO4
2.56 eV
2.87 eV
2.92 eV
3.20 eV
4.11 eV
E-EF /eV
(a)
O
P
V
Sc
a
c
ScP0.5V0.5O4
(b)
ScO8
BO4
b
a
Sc
Sc···O···B
O
B = P/V
2.2702Å
2.1529Å
ScO8
PO4
ScPO4
(i)
Bi
Sc····O···P
Bi····O···P
Bi····O···V
(ii)
2.3676Å
2.1289Å
ScO8
VO4
ScVO4
(iii)
Crystal Structure
(c)

Figure 1

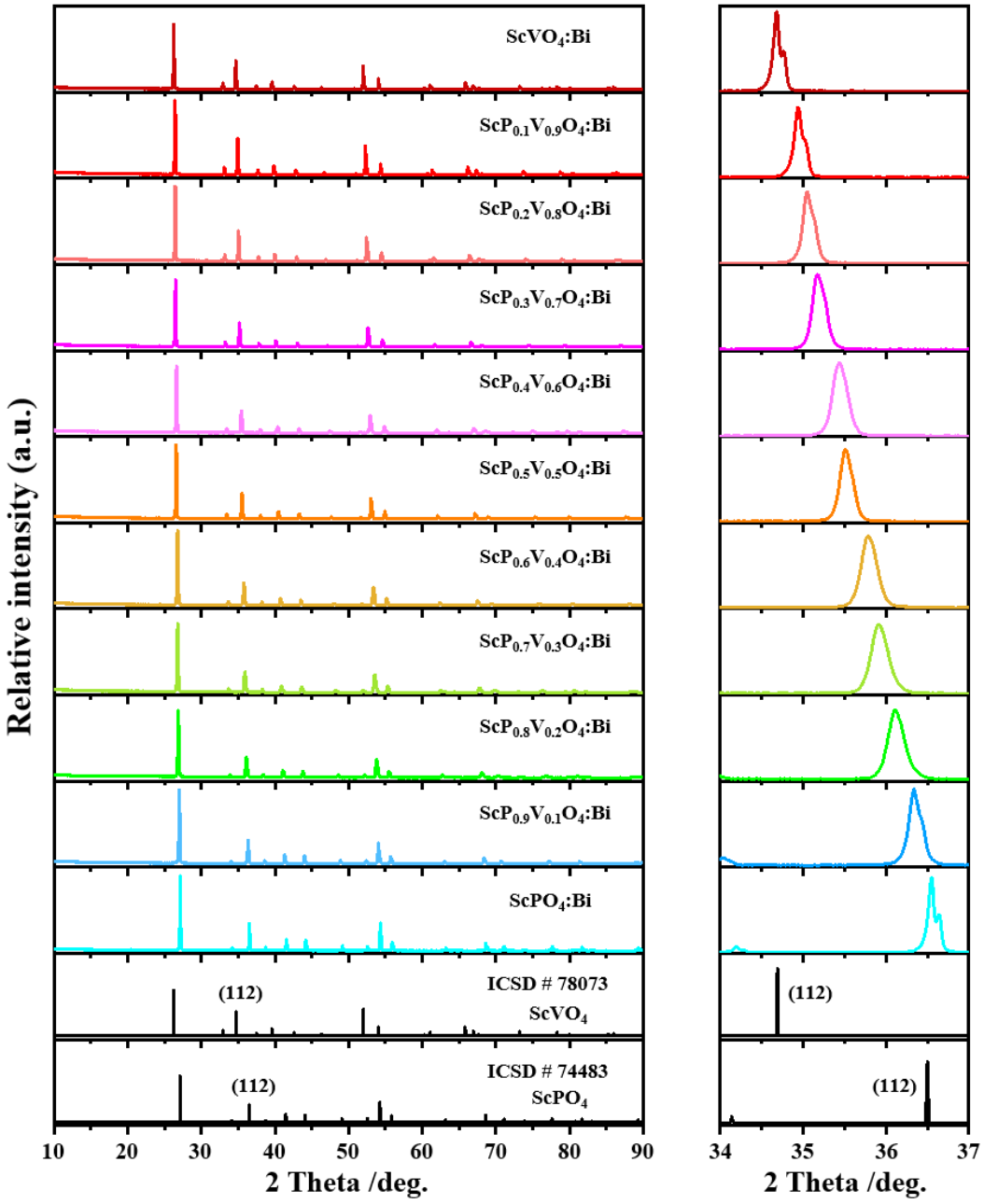
ScVO4:Bi
ScP0.1V0.9O4:Bi
ScP0.2V0.8O4:Bi
ScP0.3V0.7O4:Bi
ScP0.4V0.6O4:Bi
ScP0.5V0.5O4:Bi
ScP0.6V0.4O4:Bi
ScP0.7V0.3O4:Bi
ScP0.8V0.2O4:Bi
ScP0.9V0.1O4:Bi
ScPO4:Bi
ICSD # 78073
ScVO4
(112)
ICSD # 74483
ScPO4
(112)
Relative intensity (a.u.)
10 20 30 40 50 60 70 80 90
2 Theta /deg.
(a)
34 35 36 37
2 Theta /deg.
(b)

Figure 2

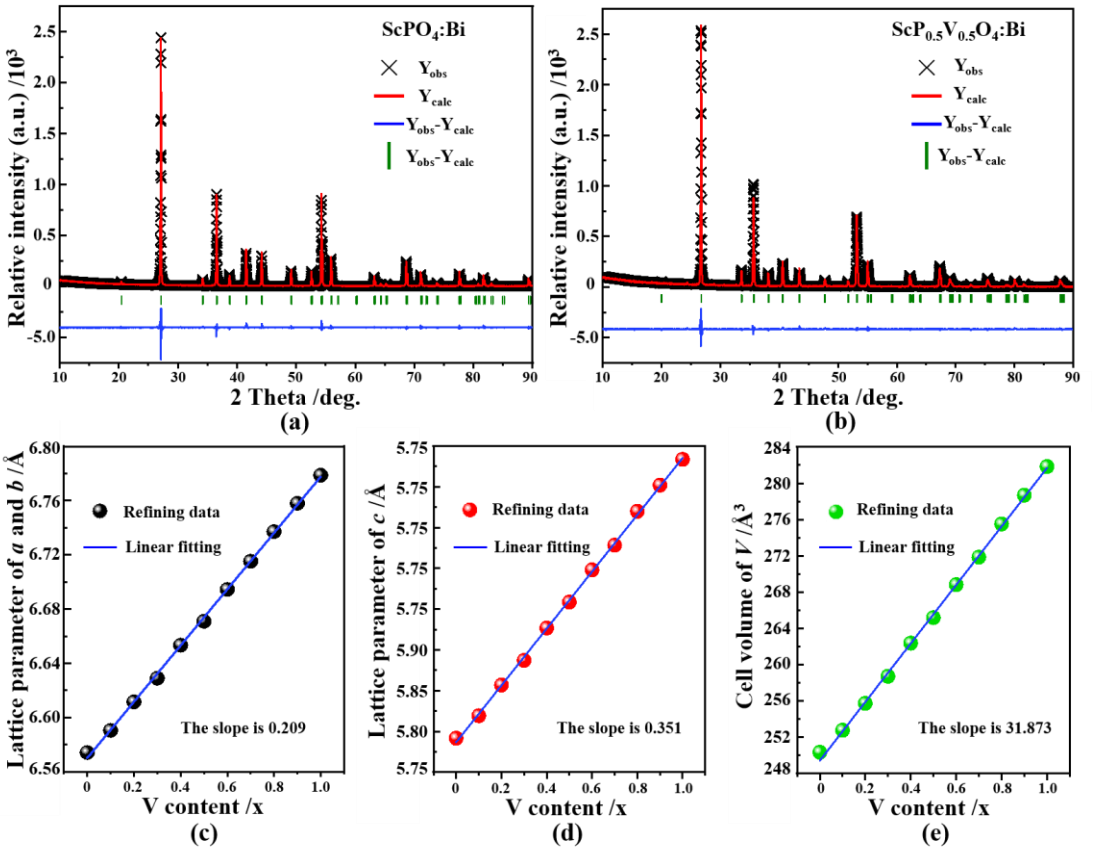
ScPO4:Bi
Yobs
Ycalc
Yobs-Ycalc
Yobs-Ycalc
Relative intensity (a.u.) /10^3
2 Theta /deg.
(a)
ScP0.5V0.5O4:Bi
Yobs
Ycalc
Yobs-Ycalc
Yobs-Ycalc
Relative intensity (a.u.) /10^3
2 Theta /deg.
(b)
Refining data
Linear fitting
The slope is 0.209
Lattice parameter of a and b /Å
V content /x
(c)
Refining data
Linear fitting
The slope is 0.351
Lattice parameter of c /Å
V content /x
(d)
Refining data
Linear fitting
The slope is 31.873
Cell volume of V /Å3
V content /x
(e)

Figure 3

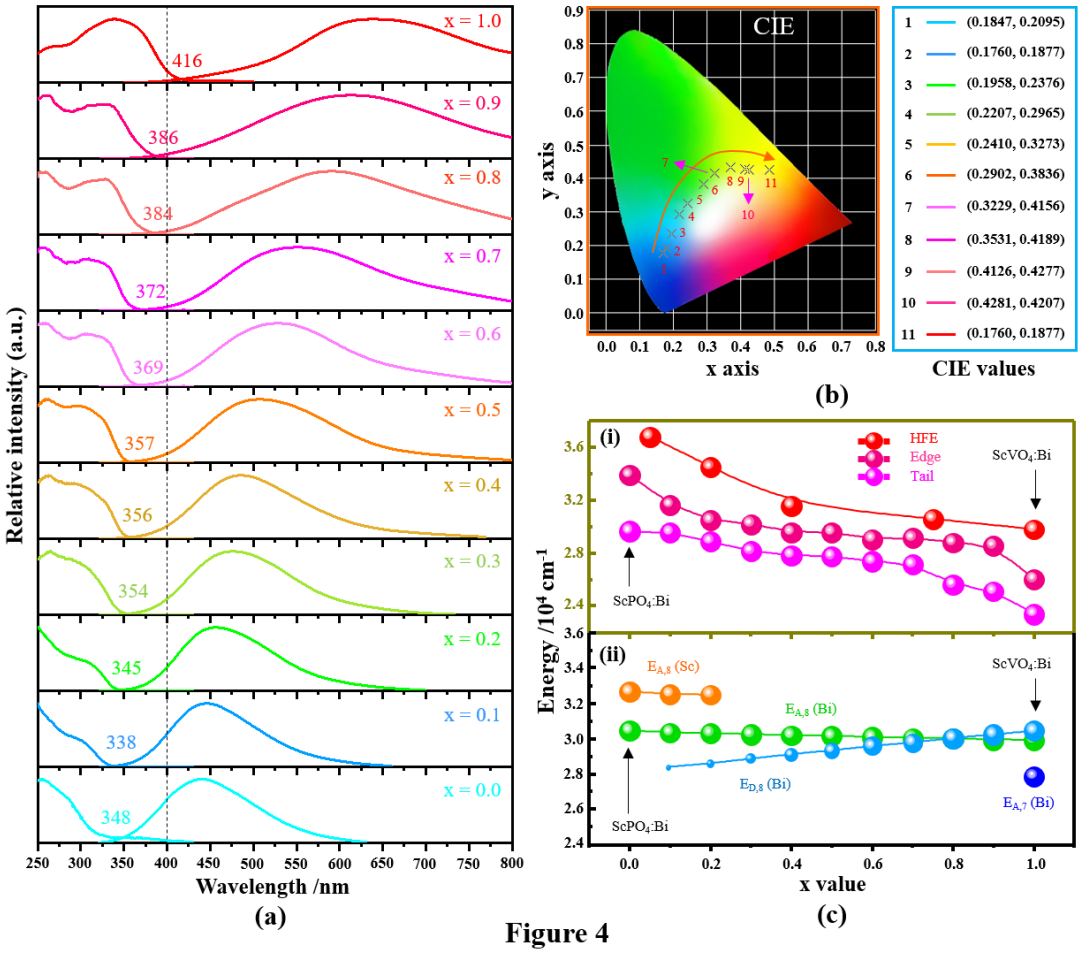
x = 1.0
416
x = 0.9
386
x = 0.8
384
x = 0.7
372
x = 0.6
369
x = 0.5
357
x = 0.4
356
x = 0.3
354
x = 0.2
345
x = 0.1
338
x = 0.0
348
Relative intensity (a.u.)
Wavelength /nm
(a)
CIE
y axis
x axis
(b)
1 (0.1847, 0.2095)
2 (0.1760, 0.1877)
3 (0.1958, 0.2376)
4 (0.2207, 0.2965)
5 (0.2410, 0.3273)
6 (0.2902, 0.3836)
7 (0.3229, 0.4156)
8 (0.3531, 0.4189)
9 (0.4126, 0.4277)
10 (0.4281, 0.4207)
11 (0.1760, 0.1877)
CIE values
(i)
HFE
Edge
Tail
ScVO4:Bi
ScPO4:Bi
(ii)
EA,8 (Sc)
EA,8 (Bi)
ED,8 (Bi)
EA,7 (Bi)
ScVO4:Bi
ScPO4:Bi
Energy /10^4 cm^-1
x value
(c)

Figure 4

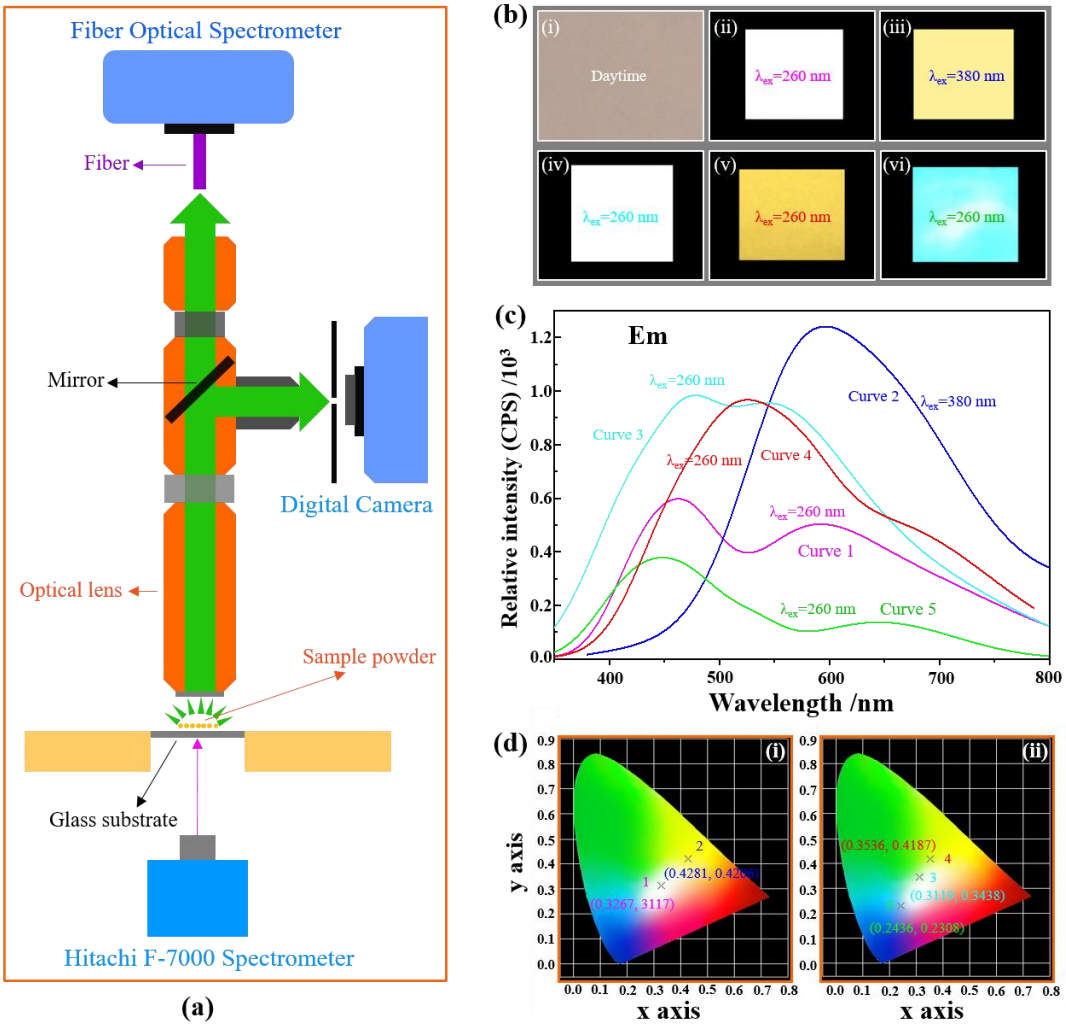
Fiber Optical Spectrometer
Fiber
Mirror
Digital Camera
Optical lens
Sample powder
Glass substrate
Hitachi F-7000 Spectrometer
(a)
(b)
(i)
Daytime
(ii)
λex=260 nm
(iii)
λex=380 nm
(iv)
λex=260 nm
(v)
λex=260 nm
(vi)
λex=260 nm
(c)
Em
Relative intensity (CPS) /10³
Wavelength /nm
Curve 1
Curve 2
Curve 3
Curve 4
Curve 5
(d)
y axis
x axis
(0.4281, 0.4206)
(0.3267, 3117)
(0.3536, 0.4187)
(0.3110, 0.3438)
(0.2436, 0.2308)

Figure 5

TOC

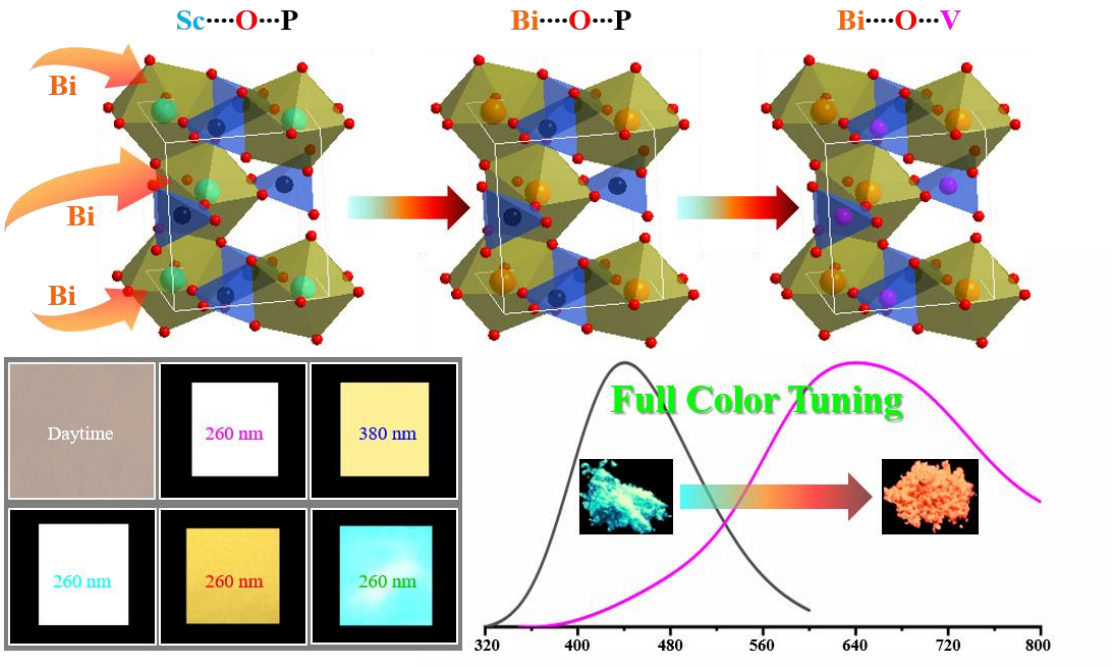
Sc····O···P
Bi····O···P
Bi····O···V
Bi
Bi
Bi
Daytime
260 nm
380 nm
260 nm
260 nm
260 nm
Full Color Tuning
320
400
480
560
640
720
800